Available online at www.sciencedirect.com
SCIENCE DIRECT®
Journal of Magnetic Resonance 175 (2005) 226–234
JMR Journal of Magnetic Resonance
www.elsevier.com/locate/jmr

Quantum logical operations for spin 3/2 quadrupolar nuclei monitored by quantum state tomography

F.A. Bonk [a], E.R. deAzevedo [a,*], R.S. Sarthour [b], J.D. Bulnes [b], J.C.C. Freitas [c], A.P. Guimarães [b], I.S. Oliveira [b], T.J. Bonagamba [a]

[a] *Instituto de Física de São Carlos, Universidade de São Paulo, Caixa Postal 369, São Carlos, 13560-970 SP, Brazil*
[b] *Centro Brasileiro de Pesquisas Físicas, Rua Dr. Xavier Sigaud 150, Rio de Janeiro, 22290-180 RJ, Brazil*
[c] *Departamento de Física, Universidade Federal do Espírito Santo, Vitória, 29060-900 ES, Brazil*

Received 8 January 2005; revised 5 April 2005
Available online 24 May 2005

Abstract

This article presents the realization of many self-reversible quantum logic gates using two-qubit quadrupolar spin 3/2 systems. Such operations are theoretically described using propagation matrices for the RF pulses that include the effect of the quadrupolar evolution during the pulses. Experimental demonstrations are performed using a generalized form of the recently developed method for quantum state tomography in spin 3/2 systems. By doing so, the possibility of controlling relative phases of superimposed pseudo-pure states is demonstrated. In addition, many aspects of the effect of the quadrupolar evolution, occurring during the RF pulses, on the quantum operations performance are discussed. Most of the procedures presented can be easily adapted to describe selective pulses of higher spin systems (>3/2) and for spin 1/2 under J couplings.

Keywords: NMR quantum computing; Quadrupolar nuclei; Logical operations; Transition-selective pulses; Density matrix

1. Introduction

Since the early demonstration that NMR systems could be used for quantum information processing, great achievement has been obtained using this technique [1–11]. Despite the exponential loss of NMR signal upon increasing number of qubits, which restricts the scalability of systems for quantum computing [12], the large number of demonstrations of quantum gates and algorithms using NMR has shown that this technique has appropriate tools for performing quantum computing. This characteristic mostly relies on the possibility of controlling with great precision the phase of quantum states through the application of radiofrequency (RF) pulses. Besides that, the recent developments for creating highly pure states and also new detection schemes are very promising for overcoming the limitations of NMR quantum computing [13–15]. In many cases, the pulse sequences used for implementing quantum gates or algorithms are performed using short hard pulses, for which the effect of the nuclear spin interactions during the pulse is negligible. Recently, new implementations of quantum logic operations using quadrupolar nuclei ($I > 1/2$) have been proposed. In these systems, a quadrupolar nucleus, such as ^{7}Li, ^{23}Na, or ^{133}Cs, diluted in a liquid crystalline matrix produces a well-defined NMR spectrum, whose line frequencies and intensities are associated with single-quantum transition frequencies and populations of quantum levels. Many applications of such systems for quantum computing NMR are available in the literature, including the creation of pseudo-pure

* Corresponding author. Fax: +55 16 33739876.
E-mail address: azevedo@if.sc.usp.br (E.R. deAzevedo).

1090-7807/$ - see front matter © 2005 Elsevier Inc. All rights reserved.
doi:10.1016/j.jmr.2005.04.009

states [16], implementation of basic quantum gates [17], and quantum algorithms [3,4,18], studies of the relaxation of coherent states [19], and also methods for performing quantum state tomography [20]. However, many of these demonstrations are based only on the spectral information, i.e., the full density matrices of the involved states are not obtained. Since many of the quantum operations involve the creation of superimposed states, whose the relative phases are characterized by off-diagonal coherences, the complete information about such states is only obtained by performing density matrix tomography, where all coherences and populations for a given state are determined. With this in mind, in this work pulse sequences for performing self-reversible Hadamard and CNOT quantum logical operations, as well as for creating a pseudo-cat state are presented and experimentally demonstrated using the density matrix tomography process. In all these applications, transition-selective pulses were used for performing quantum computation and analytical propagation matrices that represent such pulses, including the effect of the quadrupolar evolution during the pulses [21], are presented. This allowed describing the effect of the quadrupolar evolution during transition-selective pulses in the context of quantum computation and also designing experimental calibration procedures to minimize such effects.

2. Experimental procedures

The ^{23}Na NMR experiments were performed using a 9.4 T-VARIAN INOVA spectrometer in a lyotropic liquid crystal system prepared with 20.9 wt% of sodium dodecyl sulfate (95% of purity), 3.7 wt% of decanol, and 75.4 wt% of deuterium oxide, following the procedure described elsewhere [22]. ^{23}Na NMR data were recorded at room temperature using a home-built single-resonance probe with radiofrequency Helmholtz-like rectangular coils (only one loop 2.5 cm high and 1 cm wide) separated by 7.5 mm. The geometry of the coils was chosen to improve the RF magnetic field homogeneity along the sample, which was packed into a 5 mm NMR tube 0.5 cm high. Gaussian-shaped RF pulses with typical duration of 0.3–0.5 ms were used to perform selective saturation ($\pi/2$) and inversion (π) of populations. The mean RF amplitudes and the frequency offsets were carefully adjusted to satisfy the selectivity condition [23,24]. A non-selective hard $\pi/20$ pulse 1.5 μs long was applied to measure the differences of populations for the three pairs of adjacent levels. Experiments were performed with a recycle delay of 500 ms. The ^{23}Na NMR spectra were obtained by applying a reading $\pi/20$ hard pulse according to a standard CYCLOPS scheme.

3. NMR in quadrupole systems

The quantum levels in systems of diluted quadrupole nuclei are defined by the Zeeman and Quadrupolar interactions. The secular part of the Hamiltonian for this system, which defines the energy manifold, can be described in first order by Eq. (1), where ω_L is the Larmor frequency of the nucleus and ω_Q is the effective quadrupole frequency associated with the interaction between the nuclear quadrupole moment and an axially symmetric electric-field gradient [25]

$$H = -\hbar\omega_L I_z + \hbar\omega_Q(3I_z^2 - I^2). \tag{1}$$

For a spin 3/2 system, this Hamiltonian gives rise to four unequally spaced energy levels, originating an NMR spectrum containing three lines, corresponding to transitions between adjacent levels. These energy states $|3/2\rangle$, $|1/2\rangle$, $|-1/2\rangle$, and $|-3/2\rangle$ can be labeled as $|00\rangle$, $|01\rangle$, $|10\rangle$, and $|11\rangle$ in analogy to a two-qubit system [16]. From the Hamiltonian, the density matrix can be obtained according to Eq. (2), in the high temperature regime, where Z is the partition function and $\beta = 1/k_B T$

$$\rho = \frac{1}{Z}\exp(-\beta H) = \frac{1}{Z}(1 - \beta H) = \frac{1}{Z} - \Delta\rho, \tag{2}$$

where $\Delta\rho$ is a deviation density matrix. It is worth to mention that only the deviation density matrices are affected by the RF pulses and contribute to the detected NMR signal.

4. Transition-selective pulses for spin 3/2

Quantum computing procedures in quadrupolar spin systems are usually performed using transition-selective pulses and an adequate analytical description of such pulses is desirable. In the rotating frame with angular frequency ω_{RF}, the evolution operator for a RF pulse can be constructed according to [23,24,26]

$$\begin{aligned} U &= \exp\left(-\mathrm{i}\frac{H_p}{\hbar}t_p\right) \\ &= \exp\left(-\mathrm{i}\left[\Delta\omega I_z - \omega_1 I_\alpha + \frac{\omega_Q}{3}(3I_z^2 - I(I+1))\right]t_p\right). \end{aligned} \tag{3}$$

In this expression, the parameter $\Delta\omega = \omega_{RF} - \omega_L$ measures the frequency offset between the selective pulse carrier frequency (ω_{RF}) and the Larmor frequency; the strength of the RF pulse is specified by $\omega_1 = \gamma B_1$, where B_1 is the amplitude of the RF pulse; I_α is the angular momentum spin operator corresponding to a pulse with phase α ($\alpha = 0$, 1, 2, 3 for phases x, y, $-x$, $-y$, respectively); and t_p is the pulse length. An analytical representation of the pulse operator matrix can be obtained by diagonalization of the Hamiltonian, which allows the explicit evaluation of the exponential operator. For

transition-selective pulses, the condition $\omega_L \gg \omega_Q \gg \omega_1$ must be satisfied, and also the pulse must be such that $\omega_{RF} = (E_r - E_s)/\hbar$, where r and s represent the two levels connected by the selective pulse. A proper theoretical description has already been developed by Wokaun and Ernst [24], using the single-transition operator formalism. For RF pulses with B_1 field applied along the α direction, the operator I_α can be written, in terms of single-transition operators, as

$$I_\alpha = \sum_{rs} \sqrt{c^{rs}} I_\alpha^{rs}; \qquad I_z = \sum_{rs} c^{rs} I_z^{rs} \quad \text{with}$$
$$c^{rs} = I(I+1) - m_r m_s. \tag{4}$$

The operators I_α^{rs} correspond to single-transition operators connecting the energy levels r and s, as defined in [24]. Thus, for describing a selective pulse in the transition $r \to s$ with a nutation angle of θ it is necessary to set $\omega_{RF} = (E_r - E_s)/\hbar$ and $I_\alpha = \sqrt{c^{rs}} I_\alpha^{rs}$, which correspond to the case of $\omega_1 \ll \omega_Q$ [24,26]. Under this condition, the pulse operator can be rewritten as

$$U = P_\alpha^{rs}(\theta) = \exp\left(\frac{-i\theta\omega_Q}{2\omega_1}\left[\frac{\Delta\omega}{\omega_Q}\left(\sum_{ij} c^{ij} I_z^{ij}\right) - \frac{\omega_1}{\omega_Q}\sqrt{c^{rs}} I_\alpha^{rs} + \left(\left(\sum_{ij} c^{ij} I_z^{ij}\right)^2 - \frac{3}{4}\right)\right]\right). \tag{5}$$

The argument appearing in the exponential can be easily diagonalized leading to a matrix representation for the pulse operator. In the matrix representation, the pulse operators for the three allowed transitions are obtained with the choice $\Delta\omega = -2\omega_Q$, 0, $+2\omega_Q$ for transitions 01 ($|3/2\rangle \to |1/2\rangle$), 12 ($|1/2\rangle \to |-1/2\rangle$), and 23 ($|-1/2\rangle \to |-3/2\rangle$), respectively:

$$P_\alpha^{01}(\theta) = \begin{pmatrix} \cos\left(\frac{\sqrt{3}\theta}{2}\right)e^{2i\omega_Q t_p} & i\sin\left(\frac{\sqrt{3}\theta}{2}\right)e^{i\left(2\omega_Q t_p - \frac{\pi}{2}\alpha\right)} & 0 & 0 \\ i\sin\left(\frac{\sqrt{3}\theta}{2}\right)e^{i\left(2\omega_Q t_p + \frac{\pi}{2}\alpha\right)} & \cos\left(\frac{\sqrt{3}\theta}{2}\right)e^{2i\omega_Q t_p} & 0 & 0 \\ 0 & 0 & 1 & 0 \\ 0 & 0 & 0 & e^{-i4\omega_Q t_p} \end{pmatrix},$$

$$P_\alpha^{12}(\theta) = \begin{pmatrix} e^{-i\omega_Q t_p} & 0 & 0 & 0 \\ 0 & \cos\left(\frac{\theta}{2}\right)e^{i\omega_Q t_p} & i\sin\left(\frac{\theta}{2}\right)e^{i\left(\omega_Q t_p - \frac{\pi}{2}\alpha\right)} & 0 \\ 0 & i\sin\left(\frac{\theta}{2}\right)e^{i\left(\omega_Q t_p + \frac{\pi}{2}\alpha\right)} & \cos\left(\frac{\theta}{2}\right)e^{i\omega_Q t_p} & 0 \\ 0 & 0 & 0 & e^{-i\omega_Q t_p} \end{pmatrix},$$

$$P_\alpha^{23}(\theta) = \begin{pmatrix} e^{-4i\omega_Q t_p} & 0 & 0 & 0 \\ 0 & 1 & 0 & 0 \\ 0 & 0 & \cos\left(\frac{\sqrt{3}\theta}{2}\right)e^{2i\omega_Q t_p} & i\sin\left(\frac{\sqrt{3}\theta}{2}\right)e^{i\left(2\omega_Q t_p - \frac{\pi}{2}\alpha\right)} \\ 0 & 0 & i\sin\left(\frac{\sqrt{3}\theta}{2}\right)e^{i\left(2\omega_Q t_p + \frac{\pi}{2}\alpha\right)} & \cos\left(\frac{\sqrt{3}\theta}{2}\right)e^{2i\omega_Q t_p} \end{pmatrix}, \tag{6}$$

where α is the pulse phase. The pulse matrices obtained by numerical evaluation of the pulse operator using Eq. (3) are in agreement with the above ones in the limit $\omega_1 \ll \omega_Q$. It is important to notice that the non-zero elements of the pulse matrix are modulated by exponential factors, which depend on ω_Q and t_p. This effect is due to the quadrupole interaction, and the modulating factors are significant only when the term $2\pi/\omega_Q$ is comparable to the pulse duration. It is also easily recognized that for $t_p = 2\pi k/\omega_q$, where k is an integer number, the matrix representation of transition-selective pulses becomes independent of the quadrupolar frequency and reduces exactly to the representation of ideal selective pulses presented in the appendices of [5,18].

5. Effects of the quadrupolar interaction on the evolution of a spin 3/2 system

With the selective-transition pulse matrices properly defined, some general features of the evolution of a 3/2-spin system under the influence of such pulses can be addressed. Starting from a deviation density matrix, $\Delta\rho(0)$, written in a general form as

$$\Delta\rho(0) = \begin{pmatrix} a & x_a + iy_a & x_b + iy_b & x_c + iy_c \\ x_a - iy_a & b & x_d + iy_d & x_e + iy_e \\ x_b - iy_b & x_d - iy_d & c & x_f + iy_f \\ x_c - iy_c & x_e - iy_e & x_f - iy_f & d \end{pmatrix}, \tag{7}$$

the effect of a transition-selective RF pulse on such matrix can be obtained by performing the operation $\Delta\rho(t_p) = (P_\alpha^{rs}(t_p))\Delta\rho(0)(P_\alpha^{rs}(t_p))^\dagger$. After the application of a transition-selective $\pi/2$ RF pulse on the transition 01 with phase x, the deviation matrix, $\Delta\rho(t_p)$, becomes

$$\begin{pmatrix} \frac{1}{2}(aa + 2y_a + bb) & \frac{-i}{2}(aa - bb + 2ix_a) & \frac{1}{\sqrt{2}}e^{2i\omega_q t}(x_b + iy_b + ix_d - y_d) & \frac{1}{\sqrt{2}}e^{6i\omega_q t}(x_c + iy_c + ix_e - y_e) \\ \frac{i}{2}(aa - bb - 2ix_a) & \frac{1}{2}(aa + bb - 2y_a) & \frac{i}{\sqrt{2}}e^{2i\omega_q t}(x_b + iy_b - ix_d + y_d) & \frac{i}{\sqrt{2}}e^{6i\omega_q t}(x_c + iy_c - ix_e + y_e) \\ \frac{1}{\sqrt{2}}e^{-2i\omega_q t}(x_b - iy_b - ix_d - y_d) & \frac{-i}{\sqrt{2}}e^{-2i\omega_q t}(x_b - iy_b + ix_d + y_d) & c & e^{4i\omega_q t}(x_f + iy_f) \\ \frac{1}{\sqrt{2}}e^{-6i\omega_q t}(x_c - iy_c - ix_e - y_e) & \frac{-i}{\sqrt{2}}e^{-6i\omega_q t}(x_c - iy_c + ix_e + y_e) & e^{-4i\omega_q t}(x_f - iy_f) & d \end{pmatrix}. \tag{8}$$

The diagonal elements of $\Delta\rho(t_p)$ do not depend on the modulation factor, so neither the NMR spectrum, but single-, double-, and triple-quantum elements are modulated by the quadrupolar evolution. Because the implementation of logical operations usually requires multiple pulses, this can compromise the action of the pulse sequence as a logical gate. An example of this statement is the pulse sequence $(\pi)^{01}_{-y}$–$(\frac{\pi}{2})^{12}_{y}$–$(\pi)^{01}_{y}$–$(2\pi)^{01}_{-x}$. A single application of this pulse sequence to the pseudo-pure state $|00\rangle$, $U|00\rangle = P^{01}_{-x}(2\pi)P^{01}_{y}(\pi)P^{12}_{y}(\frac{\pi}{2})P^{01}_{-y}(\pi)|00\rangle$, produces the state $|\psi_1\rangle = \frac{-1}{\sqrt{2}}[|00\rangle e^{i17\omega_Q t_p} + |10\rangle e^{i5\omega_Q t_p}]$ and the application of the same pulse sequence to the state $|\psi_1\rangle$, $U|\psi_1\rangle$, produces the state $|\psi_2\rangle = \frac{1}{2}[|00\rangle(e^{i18\omega_Q t_p} + e^{i34\omega_Q t_p}) + |10\rangle(e^{i22\omega_Q t_p} - e^{i6\omega_Q t_p})]$ (see Appendix A for the corresponding density matrices). Thus, this pulse sequence only correspond to a self-reversible Hadamard operation in the first qubit, $U|00\rangle = \frac{1}{\sqrt{2}}(|00\rangle + |10\rangle)$ and $U^2|00\rangle = |00\rangle$, for the condition $t_p = 2\pi k/\omega_q$, where k is an integer number, disregarding global phases. However, this optimal pulse length may vary significantly upon experimental conditions, making important to perform calibration experiments. A calibration pulse sequence that encodes the quadrupolar evolution during the pulse in the intensity of the NMR peaks is $(\pi/2)^{12}_{y} - (\pi/2)^{01}_{x} - (\pi/2)^{12}_{y} - (\pi/20)^{\text{hard}}_{\text{cyclops}}$, where $(\pi/20)^{\text{hard}}_{\text{cyclops}}$ stands for a hard pulse applied according to the CYCLOPS detection scheme. The resulting NMR line intensities A_{01}, A_{12}, and A_{23}, corresponding, respectively, to the allowed transitions $|3/2\rangle \to |1/2\rangle$, $|1/2\rangle \to |-1/2\rangle$, and $|-1/2\rangle \to |-3/2\rangle$, after running such pulse sequence are:

$$\begin{aligned} A_{01} &= 0.65\{2e_{11}e_{12} - e_{12}e_{22} + e_{13}e_{23}\} \\ &\quad + 0.61\{e_{12}e_{22} - e_{13}e_{23}\}\cos(2\omega_Q t_p), \\ A_{12} &= 4.5e_{12}e_{13} - 1.41e_{22}e_{23}\cos(2\omega_Q t_p), \\ A_{23} &= 0.65\{2e_{13}e_{14} + e_{12}e_{22} + e_{13}e_{23}\} \\ &\quad + 0.61\{e_{12}e_{22} - e_{13}e_{23}\}\cos(2\omega_Q t_p), \end{aligned} \tag{9}$$

where e_{ij} are the matrix elements of the $(\pi/20)$ pulse operator, see [20]. Thus, because the line intensities depend on $\omega_Q t_p$, the condition $t_p = 2\pi k/\omega_Q$ can be experimentally obtained by monitoring the line intensities as a function of t_p.

6. Quantum state tomography and quadrupolar evolution

The quantum state of a spin system can only be completely characterized if all the elements of the density matrix are known, making the quantum state tomography a fundamental tool for quantum information processing. Recently, a method for performing the quantum state tomography of a quadrupolar spin 3/2 NMR system has been reported [20]. The following steps summarize the basic idea of the method. A more detailed description can be found in [20]:

(a) The diagonal elements of the deviation density matrix are determined from the intensities of the three lines measured in the averaged spectrum obtained after the application of a $\pi/20$ readout pulse applied under the CYCLOPS phase cycling scheme. Then, a set of three equations relating the matrix elements of the $\pi/20$ pulse, the diagonal elements of the density matrix a, b, c, d, and the line intensities are built. A fourth equation is obtained from the trace relation $a + b + c + d = 0$ for the deviation density matrix. Thus, the set of equations is solved to obtain a, b, c, and d.

(b) To obtain the coherences of the deviation density matrix, $\pi/2$ transition-selective pulses with proper phases are applied to the system prior to the readout pulse to drag each individual matrix element to the diagonal. Then, the same reading procedure is applied to determine the new diagonal elements, and, consequently, each element dragged to the diagonal by the transition-selective pulse. The phase and frequency of the selective pulse define which element is obtained. For single-quantum coherences one selective pulse is applied, while for double- and triple-quantum coherences two and three pulses are used, respectively.

Because the quantum state tomography method involves the application of more than one successive transition-selective pulse, it is expected that the quadrupolar evolution plays an important role in the process. Using the pulse matrices of Eq. (6) and the procedure summarized above, it is possible to obtain a set of equations, which allows determining the single-quantum elements:

$$\begin{aligned} y_a &= [\rho_{11}(P^{01}_X) - \rho_{22}(P^{01}_X)]/2, \\ y_d &= [\rho_{22}(P^{12}_X) - \rho_{33}(P^{12}_X)]/2, \\ y_f &= [\rho_{33}(P^{23}_X) - \rho_{44}(P^{23}_X)]/2, \\ x_a &= [\rho_{11}(P^{01}_Y) - \rho_{22}(P^{01}_Y)]/2, \\ x_d &= [\rho_{22}(P^{12}_Y) - \rho_{33}(P^{12}_Y)]/2, \\ x_f &= [\rho_{33}(P^{23}_Y) - \rho_{44}(P^{23}_Y)]/2, \end{aligned} \tag{10}$$

where the notation $\rho_{kk}(P^{mn}_{\alpha}\cdots P^{ij}_{\alpha'})$ stands for the diagonal elements (kth line and kth column) of the deviation density matrix after the application of the respective $P^{mn}_{\alpha}\cdots P^{ij}_{\alpha'}$ pulse sequence, from right to left. It can be observed that these equations are exactly the same as presented in [20], which reflects the fact that the diagonal elements of the density matrix after a single transition-selective pulse are not affected by the quadrupolar evolution.

Analogously, for obtaining double-quantum coherences the set of equations are:

$$
\begin{aligned}
y_b &= x_d + \frac{\sqrt{2}}{2}\cos(2\omega_q t)\left[\rho_{3,3}\left(P_X^{01}P_Y^{12}\right) - \rho_{2,2}\left(P_X^{01}P_Y^{12}\right)\right] \\
&\quad + \frac{\sqrt{2}}{2}\sin(2\omega_q t)\left[\rho_{3,3}\left(P_X^{01}P_X^{12}\right) - \rho_{2,2}\left(P_X^{01}P_X^{12}\right)\right], \\
x_b &= -y_d + \frac{\sqrt{2}}{2}\cos(2\omega_q t)\left[\rho_{2,2}\left(P_X^{01}P_X^{12}\right) - \rho_{3,3}\left(P_X^{01}P_X^{12}\right)\right] \\
&\quad + \frac{\sqrt{2}}{2}\sin(2\omega_q t)\left[\rho_{3,3}\left(P_X^{01}P_Y^{12}\right) - \rho_{2,2}\left(P_X^{01}P_Y^{12}\right)\right], \\
x_e &= -y_f + \frac{\sqrt{2}}{2}\cos(2\omega_q t)\left[\rho_{3,3}\left(P_X^{12}P_X^{23}\right) - \rho_{4,4}\left(P_X^{12}P_X^{23}\right)\right] \\
&\quad + \frac{\sqrt{2}}{2}\sin(2\omega_q t)\left[\rho_{4,4}\left(P_X^{12}P_Y^{23}\right) - \rho_{3,3}\left(P_X^{12}P_Y^{23}\right)\right], \\
y_e &= x_f + \frac{\sqrt{2}}{2}\cos(2\omega_q t)\left[\rho_{4,4}\left(P_X^{12}P_Y^{23}\right) - \rho_{3,3}\left(P_X^{12}P_Y^{23}\right)\right] \\
&\quad + \frac{\sqrt{2}}{2}\sin(2\omega_q t)\left[\rho_{4,4}\left(P_X^{12}P_X^{23}\right) - \rho_{3,3}\left(P_X^{12}P_X^{23}\right)\right].
\end{aligned}
\tag{11}
$$

Using these equations, the real and imaginary parts of double-quantum elements, x_b, x_e, y_b, and y_e, can be determined. As it can be observed, under the specific choice of the pulse duration t_p ($\omega_Q t_p = 2k\pi$) the set of Eq. (11) reduces to the set of equations used to obtain the double-quantum elements presented in [20]. The two equations used to obtain the triple-quantum elements are:

$$
\begin{aligned}
&-\sqrt{2}\left[x_f\sin(6\omega_q t) + y_f\cos(6\omega_q t)\right] + (y_c - x_e)\cos(8\omega_q t) \\
&+ (x_c + y_e)\sin(8\omega_q t) = \rho_{4,4}\left(P_X^{01}P_X^{12}P_X^{23}\right) - \rho_{3,3}\left(P_X^{01}P_X^{12}P_X^{23}\right), \\
&\sqrt{2}\left[x_f\cos(6\omega_q t) - y_f\sin(6\omega_q t)\right] + (x_c - x_e)\cos(8\omega_q t) \\
&+ (y_e - y_c)\sin(8\omega_q t) = \rho_{3,3}\left(P_Y^{01}P_Y^{12}P_Y^{23}\right) - \rho_{4,4}\left(P_Y^{01}P_Y^{12}P_Y^{23}\right).
\end{aligned}
\tag{12}
$$

The solution of this set of coupled equations for x_c and y_c gives triple-quantum elements of the density matrix. These equations are also drastically simplified with $\omega_Q t_p = 2k\pi$.

Therefore, with this generalized method all the elements in the density matrix can be obtained for any pulse duration.

7. Results and discussion

7.1. Calibration experiments

In Section 5, a calibration experiment, which encodes the quadrupolar evolution in the spectral intensities, was proposed. Fig. 1 shows the resulting experimental spectral intensities as a function of pulse duration after the application of the calibration pulse sequence. Theoretical curves obtained from Eq. (9) are also shown.

As it can be observed, the periodicity of the experimental and calculated intensities is exactly the same, confirming the $\cos(2\omega_q t_p)$ modulation as stated in Eq. (9). However, to reproduce the experimental curve it was necessary to introduce a constant phase shift, which corresponds to 7.5 μs of free evolution under the quadrupolar interaction. This was attributed to an extra evolution time, introduced by the experimental frequency shift delay (~3.5–4.0 μs in the VARIAN INOVA spectrometer) performed between each pulse. When the pulse length is such that the effect of the quadrupolar evolution during the pulse is eliminated, the line intensities of the transitions $|3/2\rangle \rightarrow |1/2\rangle$ and $|-1/2\rangle \rightarrow |-3/2\rangle$ are maximized whereas the line intensity corresponding to the transition $|1/2\rangle \rightarrow |-1/2\rangle$ is minimized. Therefore, setting the pulse length to the value corresponding to the minimum intensity for the central line, the effect of the quadrupolar evolution during the pulse is minimized. The phase shift introduced to match the theoretical and experimental curves demonstrates the importance of performing calibration experiments instead of simply choosing the optimum pulse time according to the quadrupolar frequency measured from the spectrum ($\omega_Q t_p = 2k\pi$). Therefore, the calibration procedure provides a way for adequately choosing the pulse length to minimize the effect of the quadrupolar evolution during transition-selective pulses.

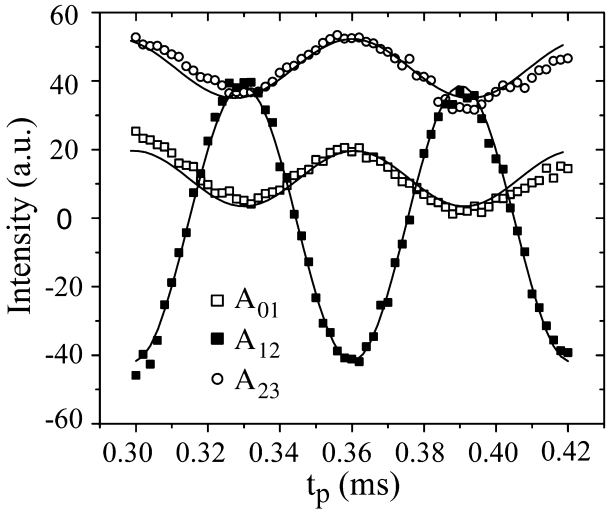

Fig. 1. Calibration curves obtained after the application of the pulse sequence $(\pi/2)_y^{12}$–$(\pi)_x^{01}$–$(\pi/2)_y^{12}$–$(\pi/20)_{\text{cyclops}}^{\text{hard}}$ to the equilibrium state. Symbols represent experimental measurements while solid lines are the curves calculated according to Eq. (9). The simulations performed using Gaussian-shaped pulses and the full Hamiltonian of Eq. (3) are identical to those calculated according to Eq. (9). In all cases, a constant phase offset corresponding to a 7.5 μs free evolution under the quadrupolar interaction was added to the simulated curves to match the experimental results.

7.2. Experimental quantum state tomography and quantum logical gates

The main desirable characteristics of a quantum state tomography process is the ability of reliably obtaining different elements of the density matrices. To demon-

strate this feature, Fig. 2 shows a bar graph of the deviation density matrices representing the selected non-normalized superposition of states $|00\rangle + |01\rangle$; $|01\rangle + |10\rangle$; $|10\rangle + |11\rangle$; $|00\rangle + |10\rangle$; $|01\rangle + |11\rangle$; and $|00\rangle + |11\rangle$, whose corresponding density matrices contain coherences of different orders. Because the imaginary parts of the deviation density matrices are zero for these states, only their real parts are shown. Such set of states are obtained from different pseudo-pure states using the pulse sequences corresponding to the following operations:

$$
\begin{aligned}
&(a) P^{01}_{-y}(\pi)P^{01}_{x}\left(\frac{\pi}{2}\right)|00\rangle = \frac{i}{\sqrt{2}}(|00\rangle + |01\rangle),\\
&(b) P^{12}_{x}(\pi)P^{12}_{-y}\left(\frac{\pi}{2}\right)|00\rangle = \frac{i}{\sqrt{2}}(|01\rangle + |10\rangle),\\
&(c) P^{23}_{x}(\pi)P^{23}_{-y}\left(\frac{\pi}{2}\right)|10\rangle = \frac{i}{\sqrt{2}}(|10\rangle + |11\rangle),\\
&(d) P^{01}_{-x}(2\pi)P^{01}_{y}(\pi)P^{12}_{y}\left(\frac{\pi}{2}\right)P^{01}_{-y}(\pi)|00\rangle = \frac{-1}{\sqrt{2}}(|00\rangle + |10\rangle),\\
&(e) P^{01}_{-x}(2\pi)P^{12}_{y}(\pi)P^{23}_{y}\left(\frac{\pi}{2}\right)P^{12}_{-y}(\pi)|01\rangle = \frac{-1}{\sqrt{2}}(|01\rangle + |11\rangle),\\
&(f) P^{12}_{x}(\pi)P^{23}_{x}(\pi)P^{12}_{x}(\pi)P^{01}_{x}(\pi)P^{01}_{y}\left(\frac{\pi}{2}\right)|00\rangle = \frac{1}{\sqrt{2}}(|00\rangle + |11\rangle).
\end{aligned}
\tag{13}
$$

It is easily recognized that the operations in Eqs. (13a), (13c), (13d), and (13e) are Hadamard transformations at different qubits, while of Eqs. (13b) and (13f) the pulse sequence creates simulations of entangled states. The global phases are not relevant because they do not appear in the corresponding density matrices. However, note that the minus signal for the density matrix shown in Fig. 2C appears because the levels $|-1/2\rangle$, $|-3/2\rangle$ are depleted in population (see [17]).

The importance of using calibrated transition-selective pulses to eliminate the quadrupolar evolution becomes clear in Fig. 3. In this case, the deviation density matrices are obtained after applying the pulse sequence $(\pi)^{12}_{-y} - (\pi/2)^{23}_{y} - (\pi)^{12}_{y} - (2\pi)^{01}_{-x}$ (Eq. (13e)) to the pseudo-pure state $|11\rangle$ with (Fig. 3A) and without (Fig. 3B) pulse optimization. While the diagonal elements are the same, the non-diagonal elements $\Delta\rho_{34}$ and $\Delta\rho_{43}$ change according to the pulse length. For the optimized pulse length ($t_p = 360$ μs in the experimental spectrum), $\Delta\rho_{34}$ and $\Delta\rho_{43}$ are purely real, and the deviation density matrix corresponding to the pseudo-pure state $|01\rangle - |11\rangle$ is obtained. On the other hand, for a pulse length of $t_p = 356$ μs the imaginary parts of the deviation density matrix clearly do not vanish. Thus, a true Hadamard Quantum gate on the qubit A is only obtained using the optimal pulse length. For all experimental deviation density matrices, the tomography processes were optimized to avoid the effects of the

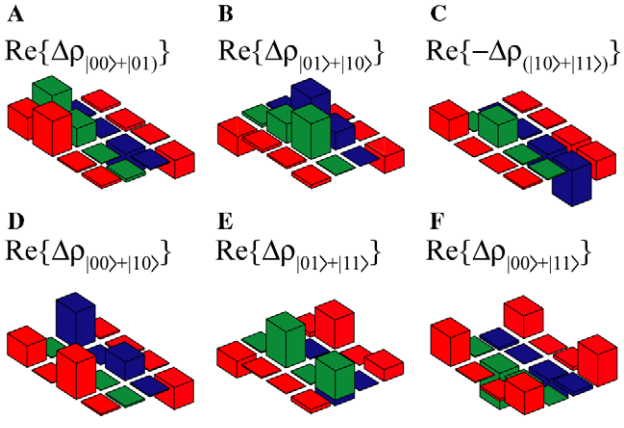

Fig. 2. Experimental deviation density matrices of several quantum states containing quantum coherences of different orders. In all cases, the tomography method was performed using Eqs. (10), (11), and (12) with transition-selective pulses optimized to avoid the effect of the quadrupolar evolution according to the procedure described in the text.

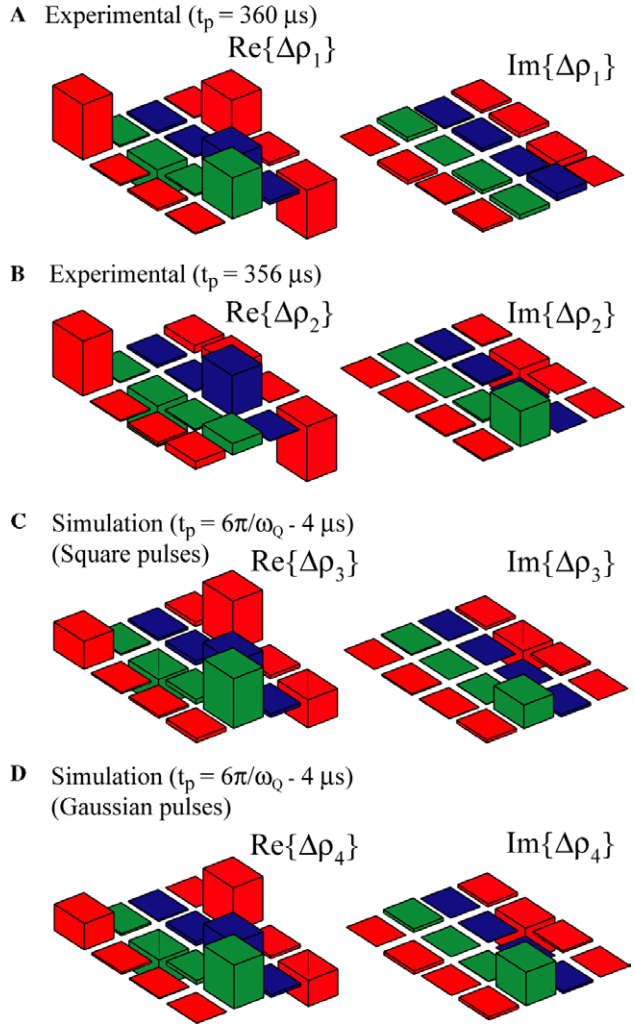

Fig. 3. Example of the quadrupolar evolution effect on the execution of a quantum gate that obtains the state $(|01\rangle - |11\rangle)$ from the state $|11\rangle$. For the optimized pulse length ($t_p = 360$ μs in the experimental spectrum), the deviation density matrices have only real non-zero elements, while for another pulse length ($t_p = 356$ μs) some non-diagonal imaginary elements show up.

quadrupolar evolution and the effect discussed above only corresponds to the execution of the gate.

Additionally, Fig. 3 shows the simulation of the corresponding states performed using square-shaped and Gaussian-shaped selective pulses. In both cases, non-optimized pulse lengths ($t_p = 6\pi/\omega_Q - 4\ \mu s$) were used in the simulation. Notice that the results obtained for square- and Gaussian-shaped pulses, and with the matrices of Eq. (6) are rather similar, confirming the validity of the theoretical description even if Gaussian pulses are used in the experiments.

The ability of reliably executing quantum state tomography allows performing many applications, for instance checking the execution of different quantum operations. The pulse sequence and the corresponding operator that executes the CNOT gate with control in the qubit A ($CNOT_A$) and B ($CNOT_B$) are:

$$\begin{aligned}
&\mathrm{CNOT}_A - \textit{Pulse Seq}\text{:}\quad (\pi)_x^{23} \qquad \textit{CNOT}_B - \textit{Pulse Seq}\text{:}\quad (\pi)_x^{12} - \pi_x^{23} - (\pi)_x^{12},\\
&U_{\mathrm{CNOT}_A}|00\rangle = P_x^{23}(\pi)|00\rangle = |00\rangle \qquad U_{\mathrm{CNOT}_B}|00\rangle = P_x^{12}(\pi)P_x^{23}(\pi)P_x^{12}(\pi)|00\rangle = |00\rangle,\\
&U_{\mathrm{CNOT}_A}|01\rangle = P_x^{23}(\pi)|01\rangle = |01\rangle \qquad U_{\mathrm{CNOT}_B}|01\rangle = P_x^{12}(\pi)P_x^{23}(\pi)P_x^{12}(\pi)|01\rangle = -|11\rangle,\\
&U_{\mathrm{CNOT}_A}|10\rangle = P_x^{23}(\pi)|10\rangle = \mathrm{i}|11\rangle \qquad U_{\mathrm{CNOT}_B}|10\rangle = P_x^{12}(\pi)P_x^{23}(\pi)P_x^{12}(\pi)|10\rangle = -|10\rangle,\\
&U_{\mathrm{CNOT}_A}|11\rangle = P_x^{23}(\pi)|11\rangle = \mathrm{i}|10\rangle \qquad U_{\mathrm{CNOT}_B}|11\rangle = P_x^{12}(\pi)P_x^{23}(\pi)P_x^{12}(\pi)|11\rangle = -|01\rangle.
\end{aligned} \tag{14}$$

The ability of reliably executing quantum state tomography allows performing many applications, for instance checking the execution of different quantum operations. The pulse sequence and the corresponding operator that executes the CNOT gate with control in the qubit A ($CNOT_A$) and B ($CNOT_B$) are:

$$\begin{aligned}
P_x^{01}(\pi)P_{-y}^{01}\left(\frac{\pi}{2}\right)|00\rangle &= \frac{\mathrm{i}}{\sqrt{2}}(|00\rangle + |01\rangle),\\
P_x^{01}(\pi)P_{-y}^{01}\left(\frac{\pi}{2}\right)|01\rangle &= \frac{\mathrm{i}}{\sqrt{2}}(|00\rangle - |01\rangle),\\
P_x^{12}(\pi)P_{-y}^{12}\left(\frac{\pi}{2}\right)|01\rangle &= \frac{\mathrm{i}}{\sqrt{2}}(|01\rangle + |10\rangle),\\
P_x^{12}(\pi)P_{-y}^{12}\left(\frac{\pi}{2}\right)|10\rangle &= \frac{\mathrm{i}}{\sqrt{2}}(|01\rangle - |10\rangle),\\
P_x^{23}(\pi)P_{-y}^{23}\left(\frac{\pi}{2}\right)|10\rangle &= \frac{\mathrm{i}}{\sqrt{2}}(|10\rangle + |11\rangle),\\
P_x^{23}(\pi)P_{-y}^{23}\left(\frac{\pi}{2}\right)|11\rangle &= \frac{\mathrm{i}}{\sqrt{2}}(|10\rangle - |11\rangle).
\end{aligned} \tag{15}$$

Fig. 4 shows a set of tomographed deviation density matrices obtained after the execution of a controlled not (CNOT) quantum gate with control in both qubits. The transformation of the states according to the action of the CNOT gate is easily recognized, showing that with the above pulse sequences the gate can be executed with very good reliability. Again, the minus signal in labeling of the deviation density matrix indicates that the level corresponding to the state is depleted in population.

Another crucial feature in quantum computing NMR is the ability of controlling and detecting relative phases of quantum states. This can be demonstrated by applying the pulse sequences that performed the operations shown in Eqs. (13a), (13b), and (13c) to different pseudo-pure states, i.e.,

Fig. 5 shows the deviation matrices of the states created after applying the corresponding pulse sequences. The set of operations shown in Figs. 5A and 5C constitutes a full Hadamard operation in the second qubit, while in Fig. 5B the resulting state is a simulation of an entangled state. The possibility of detecting and controlling relative phases is clearly shown in the tomographed deviation density matrices. It is interesting to observe that the NMR spectra obtained after applying each pulse sequence of the gate followed by $\pi/20$ readout pulse are essentially identical, indicating the impos-

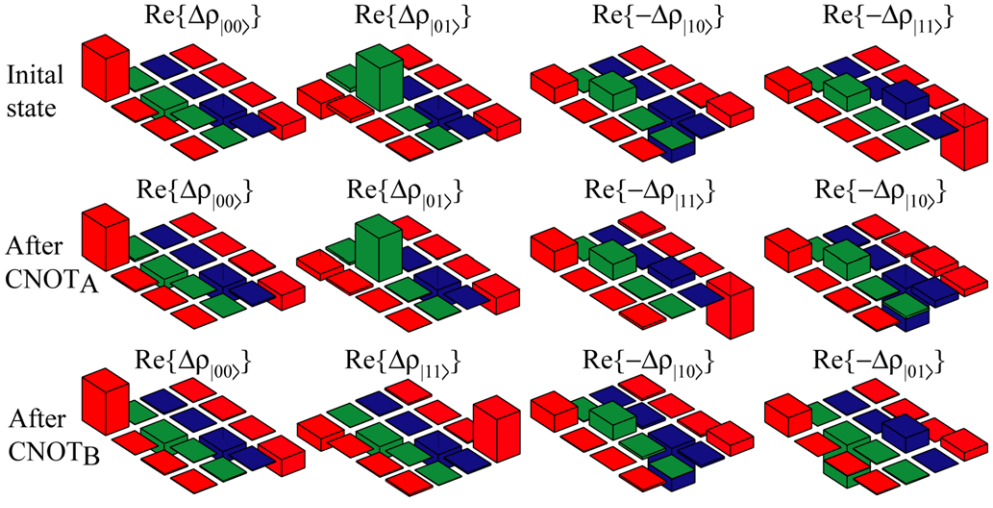

Fig. 4. Set of experimentally tomographed deviation density matrices corresponding to truth tables for CNOT's gates (for both qubits).

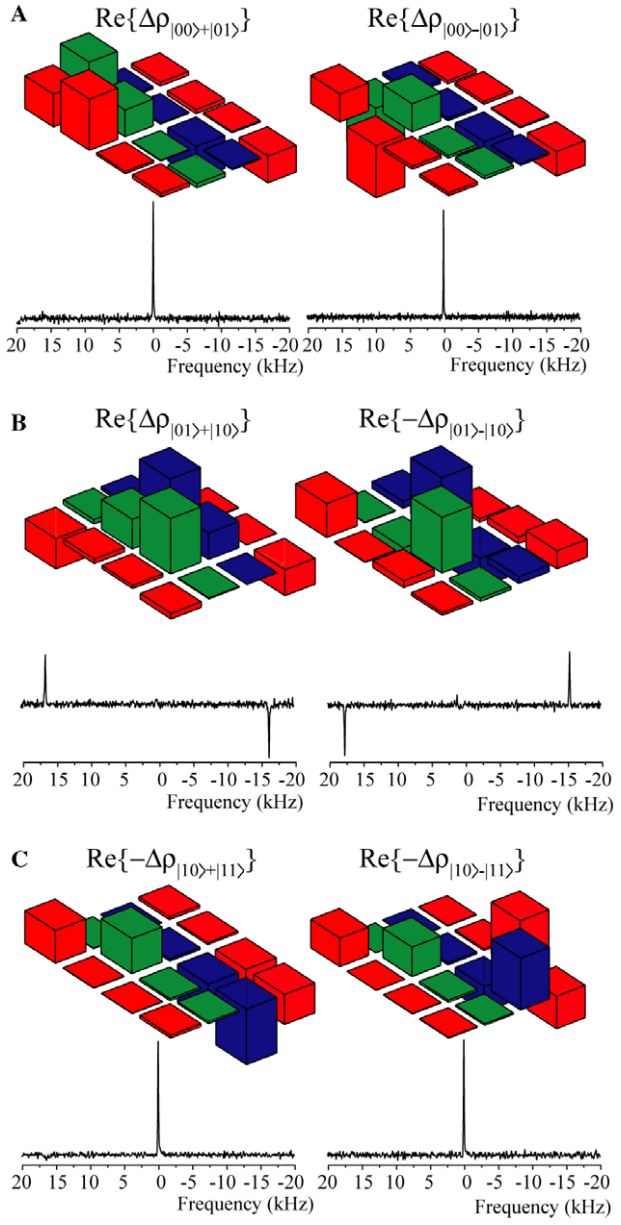

Fig. 5. Deviation density matrices representing superposition of states with different relative phases.

sibility of obtaining relative phases from the NMR spectrum. The inversion of the spectral intensities in Fig. 5B is due to the population depletion in the corresponding levels, which is not associated to the relative phases. The phase manipulation shown in Fig. 5 guarantees that the presented gates are self-reversible, i.e., if the same pulse sequence is applied to the superposition of states the initial state is recovered.

8. Conclusions

It is shown that the effect of the quadrupolar evolution during transition-selective pulses is extremely relevant for the implementation of quantum logical operations in quadrupolar systems. The importance of this effect was experimentally demonstrated using a two-qubit spin 3/2 system. Using matrix representation of the propagation operators for describing the RF pulses, it was possible to develop a calibration pulse sequence that encodes the effect of the quadrupolar evolution during the pulses in the NMR line intensities. This allowed to stablish of a relationship between the parameters that describe the RF pulse. Thus, it was possible to find an optimal pulse length that effectively minimizes the effect of the quadrupolar interaction during transition-selective pulses.

Experimental deviation density matrices of several quantum states containing quantum coherences of different orders were obtained using transition-selective pulses optimized to avoid the effect of the quadrupolar evolution (see Figs. 2 and 3). In addition, truth tables for the CNOT (for both qubits) gates were constructed using experimentally tomographed deviation density matrices. Furthermore, the new proposed calibration of the RF selective pulses allowed the correct measurement of the off-diagonal coherences for several quantum superpositions of states, as well as reliable determination of their corresponding relative phases.

All the numerical simulations performed using Gaussian-shaped pulses and the full Hamiltonian produced identical results as that ones performed using the derived pulse operators, as can be seen in Fig. 3. All the experimental results are in agreement with theoretical predictions for this particular system. Most of the procedures presented can be easily adapted to describe selective pulses in the case of higher spin systems (>3/2) and even for coupled spin 1/2 nuclei, where such pulses may be also applied to perform quantum operations.

Acknowledgments

The authors acknowledge support from CAPES, CNPq, and FAPESP. R.S.S. especially acknowledges the Brazilian Quantum Information—CNPq project—and the CAPES Pro-doc grant program. A special thank for Dr. E.L.G. Vidoto for constructing the NMR probe, and for Prof. E.A. Oliveira and Dr. D.T. Balogh for the help with the sample preparation.

Appendix A. Calculated deviation density matrices using the developed pulse matrices

(a) After the application of the pulse sequence $(\pi)^{01}_{-y} - (\pi/2)^{12}_{y} - (\pi)^{01}_{y} - (2\pi)^{01}_{-x}$ to the pseudo-pure state $|00\rangle$

$$\Delta\rho = \begin{pmatrix} +\frac{1}{2} & 0 & e^{i12\omega_Q t_p} & 0 \\ 0 & -\frac{1}{2} & 0 & 0 \\ e^{-i12\omega_Q t_p} & 0 & +\frac{1}{2} & 0 \\ 0 & 0 & 0 & -\frac{1}{2} \end{pmatrix}.$$

(b) After the application of the pulse sequence $(\pi)^{01}_{\bar{y}} - (\pi/2)^{12}_{y} - (\pi)^{01}_{y} - (2\pi)^{01}_{-x} - (\pi)^{01}_{-y} - (\pi/2)^{12}_{y} - (\pi)^{01}_{y} - (2\pi)^{01}_{-x}$ to the pseudo-pure state $|00\rangle$

$$\Delta\rho_{|00\rangle+|10\rangle} = \begin{pmatrix} \cos(16\omega_Q t_p)+\frac{1}{2} & 0 & -\frac{1}{2}(e^{-i4\omega_Q t_p} - e^{i28\omega_Q t_p}) & 0 \\ 0 & -\frac{1}{2} & 0 & 0 \\ \frac{1}{2}(e^{i4\omega_Q t_p} - e^{-i28\omega_Q t_p}) & 0 & -\cos(16\omega_Q t_p)+\frac{1}{2} & 0 \\ 0 & 0 & 0 & -\frac{1}{2} \end{pmatrix}.$$

References

[1] I.L. Chuang, N. Gershenfeld, M. Kubinec, Experimental implementation of fast quantum searching, Physical Review Letters 80 (1998) 3408–3411.

[2] D.G. Cory, M.D. Price, T.F. Havel, Nuclear magnetic resonance spectroscopy: an experimentally accessible paradigm for quantum computing, Physica D 120 (1998) 82–101.

[3] R. Das, T.S. Mahesh, A. Kumar, Experimental implementation of Grover's search algorithm using efficient quantum state tomography, Chemical Physics Letters 369 (2003) 8–15.

[4] K. Dorai, Arvind, A. Kumar, Implementation of a Deutsch-like quantum algorithm utilizing entanglement at the two-qubit level on an NMR quantum-information processor, Physical Review A 63 (2001), 034101-1–4.

[5] N.A. Gershenfeld, I.L. Chuang, Bulk spin-resonance quantum computation, Science 275 (1997) 350–356.

[6] J.A. Jones, Progress in nuclear magnetic resonance spectroscopy, Liquid-State NMR Quantum Computing 38 (2001) 325.

[7] E. Knill, I. Chuang, R. Laflamme, Effective pure states for bulk quantum computation, Physical Review A 57 (1998) 3348–3363.

[8] D. Leung, L. Vandersypen, X.L. Zhou, M. Sherwood, C. Yannoni, M. Kubinec, I. Chuang, Experimental realization of a two-bit phase damping quantum code, Physical Review A 60 (1999) 1924–1943.

[9] G.L. Long, H.Y. Yan, Y.S. Li, C.C. Tu, J.X. Tao, H.M. Chen, M.L. Liu, X. Zhang, J. Luo, L. Xiao, X.Z. Zeng, Experimental NMR realization of a generalized quantum search algorithm, Physics Letters A 286 (2001) 121–126.

[10] M.A. Nielsen, I. Chuang, Quantum Computation and Quantum Information, Cambridge University Press, Cambridge, 2002.

[11] L.M.K. Vandersypen, M. Steffen, G. Breyta, C.S. Yannoni, M.H. Sherwood, I.L. Chuang, Experimental realization of Shor's quantum factoring algorithm using nuclear magnetic resonance, Nature 414 (2001) 883–887.

[12] W.S. Warren, The usefulness of NMR quantum computing, Science 277 (1997) 1688–1689.

[13] D. Rugar, R. Budakian, H.J. Mamin, B.W. Chui, Single spin detection by magnetic resonance force microscopy, Nature 430 (2004) 329–332.

[14] M.S. Anwar, D. Blazina, H.A. Carteret, S.B. Duckett, T.K. Halstead, J.A. Jones, C.M. Kozak, R.J.K. Taylor, Preparing high purity initial states for nuclear magnetic resonance quantum computing, Physical Review Letters 93 (2004), art no. 040501.

[15] P. Hubler, J. Bargon, S.J. Glaser, Nuclear magnetic resonance quantum computing exploiting the pure spin state of para hydrogen, Journal of Chemical Physics 113 (2000) 2056–2059.

[16] A.K. Khitrin, B.M. Fung, Nuclear magnetic resonance quantum logic gates using quadrupolar nuclei, Journal of Chemical Physics 112 (2000) 6963–6965.

[17] N. Sinha, T.S. Mahesh, K.V. Ramanathan, A. Kumar, Toward quantum information processing by nuclear magnetic resonance: pseudopure states and logical operations using selective pulses on an oriented spin 3/2 nucleus, Journal of Chemical Physics 114 (2001) 4415–4420.

[18] R. Das, A. Kumar, Use of quadrupolar nuclei for quantum-information processing by nuclear magnetic resonance: implementation of a quantum algorithm, Physical Review A 68 (2003), 032304-1–8.

[19] R.S. Sarthour, E.R. deAzevedo, F.A. Bonk, E.L.G. Vidoto, T.J. Bonagamba, A.P. Guimaraes, J.C.C. Freitas, I.S. Oliveira, Relaxation of coherent states in a two-qubit NMR quadrupole system, Physical Review A 68 (2003), 022311-1–7.

[20] F.A. Bonk, R.S. Sarthour, E.R. deAzevedo, J.D. Bulnes, G.L. Mantovani, J.C.C. Freitas, T.J. Bonagamba, A.P. Guimarães, I.S. Oliveira, Quantum state tomography for quadrupole nuclei and its applications on a two-qubit system, Physical Review A 69 (2004), 042322-1–9.

[21] H. Kampermann, W.S. Veeman, Quantum computing using quadrupolar spins in solid state NMR quantum information processing, Quantum Information Processing 1 (2002) 327–344.

[22] K. Radley, L.W. Reeves, A.S. Tracey, Effect of counterion substitution on type and nature of nematic lyotropic phases from nuclear magnetic-resonance studies, Journal of Physical Chemistry 80 (1976) 174–182.

[23] S. Vega, A. Pines, Operator formalism for double quantum NMR, Journal of Chemical Physics 66 (1977) 5624–5644.

[24] A. Wokaun, R.R. Ernst, Selective excitation and detection in a multilevel spin system: application of single transition operators, Journal of Chemical Physics 67 (1977) 1752–1758.

[25] C. Slichter, Principles of Nuclear Magnetic Resonance, Springer-Verlag, New York, 1990.

[26] R.R. Ernst, G. Bodenhausen, A. Wokaun, Principles of Nuclear Magnetic Resonance in One and Two Dimensions, Clarendon Press, Oxford, 1987.